Charge flow model for atomic ordering in nonisovalent alloys

Shuzhi Wang and Lin-Wang Wang

Phys. Rev. B **83**, 115208 — Published 28 March 2011

DOI: 10.1103/PhysRevB.83.115208

Charge Flow Model for Atomic Ordering in Nonisovalent Alloys

Shuzhi Wang* and Lin-Wang Wang
Materials Sciences Division, Lawrence Berkeley National Laboratory, Mail Stop 66, One Cyclotron Rd, Berkeley, CA 94720

Nonisovalent alloys, also known as aliovalent alloys, are formed by mixing two semiconductors of different valences for both cations and anions. These alloys exhibit many interesting properties and have found applications in optoelectronics, refractory materials, photovoltaics, photocatalytic splitting of water, etc. For example, the alloy of GaN and ZnO has a surprisingly large band gap bowing, enabling visible light absorption and overall water splitting at a record quantum efficiency. The understanding of the properties of nonisovalent alloys, however, is hindered by the lack of knowledge of the detailed atomic structures. We recently developed a charge flow model which can predict the total energy of different atomic configurations of nonisovalent alloys. In this work, we extend this model and apply it to a number of alloy systems—GaN/ZnO, GaAs/ZnSe, InP/CdS, AlN/ZnO, AlN/MgO, and AlN/SiC in wurtzite, zinc-blende, and/or rocksalt structures. Good agreement between the model-predicted and *ab initio* results is found. We also employ the charge flow model in parallel tempering Monte Carlo simulations to calculate the thermodynamic properties of nonisovalent alloys of wurtzite structure. A phase transition between the phase separated and alloying regions is found and a general phase diagram is obtained. This model could be used to guide the design and synthesis of new nonisovalent alloy materials.

PACS numbers:

I. INTRODUCTION

Nonisovalent semiconductor alloys of AX and BY have shown great potentials in a variety of applications.[1–8] For nonisovalent, we mean A has a valence different from B, and X from Y (e.g., III-V AX with II-VI BY). The attraction of nonisovalent alloys lies in the ability of tuning material properties (e.g., lattice parameters, band gap, effective mass) between or even beyond those of the parent semiconductors by controlling their compositions and extent of mixing (e.g., with short range order or not).[1–7,9] It is possible that the tunability of those properties for nonisovalent alloys is larger than the conventional isovalent alloys.[8,10–12] For example, the GaN/ZnO alloy has one of the highest quantum efficiencies of overall water splitting under visible light,[4,5] which has been attributed partly to the alloying-induced band gap reduction from 3.4 eV to 2.6 eV. Another example is the alloy of SiC with AlN which displays better mechanical properties than both pure SiC and AlN.[1,6]

There are two important questions to be answered in the study of a nonisovalent alloy system AX/BY: what is the atomic structure of the alloy at a certain temperature? And what are the corresponding electronic properties? As indicated by X-ray diffraction experiments,[1,3,4] alloys of isostructural binary semiconductors usually have the same crystal structure, while that of alloys of heterostructural materials will change from one to the other at a certain composition.[13] The atomic ordering in the alloy, i.e., the configuration of the four types of atoms on the lattice sites, which plays an important role in determining the electronic properties,[2,14–17] however, is only known qualitatively from experiments,[18] which indicate a preference of bonding between atoms from the same base material. To give a quantitative answer to the question of the atomic ordering requires the knowledge of the temperature dependence of the free energy of mixing, $\Delta G_{mix} = \Delta H_{mix} - T\Delta S_{mix}$, where ΔH_{mix} and ΔS_{mix} are the enthalpy and entropy of mixing AX and BY respectively. A positive ΔG_{mix} leads to phase separation while a negative value means good mixing of AX and BY. If the mixing enthalpy ΔH_{mix} is positive, the formation of alloys is only possible above the miscibility temperature $T = \Delta H_{mix}/\Delta S_{mix}$; while a negative ΔH_{mix} will induce alloying with ordering at low temperature and with disorder at high temperature. In previous experiments, high temperatures are needed in the synthesis of GaN/ZnO (>1000 K)[4,5] and AlN/SiC (>1800 K),[1] thus indicating a positive ΔH_{mix} for these systems.

Theoretically, the thermodynamic properties of nonisovalent alloys can be obtained by Monte Carlo (MC) simulations, provided that a total energy model is readily available to carry out the simulations. The density functional theory (DFT) can calculate the energy of a given alloy configuration quite accurately, but with a rather heavy computational cost, thus rendering this approach unsuitable to be used with MC simulations. Several groups have tried to use special quasirandom structures (SQS)[19] constructed in small supercells in DFT calculations to study GaN/ZnO alloys.[15,16] The validity of using SQS in nonisovalent alloy systems, however, is questionable, as indicated by the much higher energy of those random structures compared to those with Zn and O atoms bonded together.[15,16] Our previous calculations[9] on GaN/ZnO alloys have shown that Zn prefers to bond with O to form ZnO clusters of subnano size at the synthesis temperature (1100 K), which is consistent with a recent EXAFS experiment.[18]

An alternative approach to calculate the alloy total energy is to use an empirical model which can be fitted to DFT results. The valence force field method[20–27] and the cluster expansion method[28–32] have been widely used for isovalent alloys. Electrostatic interaction models were used to study the energy of ground-state and random structures of binary and pseudobinary alloys.[33,34] Osorio et al[35] studied the atomic ordering of GaAs/Ge and GaP/Si alloys with a model Hamiltonian including electrostatic

interactions and cluster expansion components. A coulomb lattice gas model[36–40] has been applied to semiconductor alloys with nonisovalent cations, such as $Ba(Mg_{1/3}Nb_{2/3})O_3$[38] and $(AgSbTe)_x(PbTe)_{1-x}$.[40] In our previous work on GaN/ZnO,[9] we developed a charge flow model, which is based on the principle of local charge balance and has a much simpler form than the cluster expansion method, but can describe the *ab initio* total energy of GaN/ZnO alloy configurations very accurately. The equilibrium atomic configurations of GaN/ZnO containing over a thousand atoms were then investigated using parallel tempering MC (PTMC) simulations with the charge flow model and the electronic structures of equilibrated configurations were calculated using DFT with a semiempirical method to correct the DFT band gap error.[9] In the present work, we extended the charge flow model and applied it to a number of other nonisovalent alloy systems for which good agreement with direct DFT results was obtained. We then used the parameterized model Hamiltonian in PTMC simulations and obtained a general phase diagram for nonisovalent alloys of wurtzite (WZ) structure.

II. METHODS

The enthalpy of mixing AX and BY can be decomposed into three components,[41]

$$\Delta H_{mix} = \Delta E_{def} + \Delta E_{chem} + \Delta E_{rel}. \tag{1}$$

Each term represents a step in the fictitious reaction path from the bulk constituents to the final alloy: 1) deformation of the unit cell of each bulk material $S = AX$, BY from its equilibrium lattice parameters $\{\mathbf{a}_i^S\}$, $i = 1, 2, 3$, to those of the alloy $\{\mathbf{a}_i(x)\}$ of AX composition x; 2) mixing of the deformed AX and BY on the ideal lattice sites without relaxation; 3) relaxation of the internal atomic positions in the alloy structure. The first component (deformation energy ΔE_{def}) depends on the alloy lattice parameters and composition,

$$\begin{aligned}\Delta E_{def} = &[xE_{AX}(\{\mathbf{a}_i(x)\}) + (1-x)E_{BY}(\{\mathbf{a}_i(x)\})] \\ &-[xE_{AX}(\{\mathbf{a}_i^{AX}\}) + (1-x)E_{BY}(\{\mathbf{a}_i^{BY}\})],\end{aligned} \tag{2}$$

where $E_S(\{\mathbf{a}_i\})$ is the energy of system S at lattice parameters $\{\mathbf{a}_i\}$. The second term in Eq. 1 (chemical exchange energy ΔE_{chem}) describes the change in chemical interactions during alloying without internal relaxation, i.e., the energy change introduced by replacing some A–X and B–Y bonds by A–Y and B–X bonds:

$$\begin{aligned}\Delta E_{chem} \;=\; & E^{unrel}_{AX\text{-}BY}(\{\mathbf{a}_i(x)\}) - [xE_{AX}(\{\mathbf{a}_i(x)\}) \\ & +(1-x)E_{BY}(\{\mathbf{a}_i(x)\})],\end{aligned} \tag{3}$$

where $E^{unrel}_{AX\text{-}BY}(\{\mathbf{a}_i(x)\})$ is the energy at lattice parameters $\{\mathbf{a}_i(x)\}$ with atoms at the ideal unrelaxed lattice sites for a given alloy atomic configuration σ (i.e., which atom is at which site). In the final step, strain is reduced by internal relaxation:

$$\Delta E_{rel} = E^{rel}_{AX\text{-}BY}(\{\mathbf{a}_i(x)\}) - E^{unrel}_{AX\text{-}BY}(\{\mathbf{a}_i(x)\}), \tag{4}$$

where $E^{rel}_{AX\text{-}BY}(\{\mathbf{a}_i(x)\})$ is the energy at relaxed atomic positions.

Among the three components of the mixing enthalpy of nonisovalent alloys, the first term ΔE_{def} can be easily calculated using DFT at lattice parameters of the alloy with composition x, which can be interpolated from $\{\mathbf{a}_i^{AX}\}$ and $\{\mathbf{a}_i^{BY}\}$ using Vegard's law: $\mathbf{a}_i(x) = x\mathbf{a}_i^{AX} + (1-x)\mathbf{a}_i^{BY}$. The second and third terms, ΔE_{chem} and ΔE_{rel}, however, depend sensitively on the arrangement of the constituent atoms (A, X, B, Y) at the lattice sites. In our previous work on GaN/ZnO,[9] it has been shown that DFT results of these two terms can be predicted quite accurately by the charge flow model. Here we will give a detailed account of the model.

The charge flow model is based on the principle of local charge balance, which states that the charge on an ion must be balanced by the charges donated from all of its nearest neighboring ions of opposite sign in a stable configuration. This idea has been used in Pauling's electrostatic valence rule for ionic solids,[42] and the semiconductor electron counting rule for surface reconstruction.[43] In these previous models, the relation between local charge balance and the total energy, however, is rather qualitative, largely due to the lack of a quantitative measure of the deviation from local charge balance. In the charge flow model, we extend the principle of local charge balance to devise such a quantitative measure for structural stability and apply the model to nonisovalent alloy systems.

In the charge flow model, each cation (A or B) and anion (X or Y) are assumed to have a fixed valence charge regardless of the local atomic environment. For example, in the GaN/ZnO system, the charges can be $+3$ for Ga, $+2$ for Zn, -3 for N, and -2 for O. We require $Q_A = -Q_X$, $Q_B = -Q_Y$, and $Q_A \neq Q_B$. Note that in some complex alloys (e.g. oxides) some transition metal elements might have multiple valences. In that case, there will be an additional issue of choosing Q (e.g., to minimize the total energy) for each of such elements. In this paper, we will not discuss such cases. Each ion i will donate to each nearest neighbor ion j of opposite sign a portion of the charge, which is called "charge flow" and denoted by C_{ij} in our model. Here we

require 1) that the charge flow from ion j to i, C_{ji}, to be equal to C_{ij}, but with an opposite sign, i.e., $C_{ji} = -C_{ij}$, and 2) that the charge Q_i on each ion i is locally balanced by the sum of charge flows, C_{ji}, from the nearest neighbors j:

$$Q_i(\sigma, x) = -\sum_{i\sim j} C_{ji}(\sigma, x) = \sum_{i\sim j} C_{ij}(\sigma, x), \tag{5}$$

where the sign $\sim$ means atoms i and j are bonded (nearest neighbors to each other), x is the composition of AX in the alloy, and σ denotes the atomic configuration of the system with A, B occupying the cation sites and X, Y the anion sites. The antisite situation, i.e., cations being in anion sites and anions in cation sites, is not considered here because the energy of this kind of configurations is usually too high to have significant contribution at relevant temperature.[35] For a binary material AX or BY, the charge flow C_{ij} can be readily obtained by dividing the ion charge Q by the number of nearest neighbor ions N_{nnb}. For example, C_{ij} is ± 0.75 ($= \pm 3/4$) and ± 0.50 ($= \pm 2/4$) for GaN and ZnO of WZ structure, respectively. When AX is alloyed with BY, however, the charge flows are perturbed from the pure bulk values to adopt new values in order to satisfy the local charge balance (Eq. 5). The perturbation can be measured by the deviation of the mean charge flow square from that of the phase separated state:

$$\Delta J(\sigma, x) = J(\sigma, x) - J^*(x), \tag{6}$$

where $J(\sigma, x) = \frac{1}{N}\sum_{i=1}^{N}\sum_{i\sim j} C_{ij}^2(\sigma, x)$, and $J^*(x) = xJ_{AX} + (1-x)J_{BY}$. Here N is the number of atoms in the system, $J_S = Q_S^2/N_{nnb}^S$, and N_{nnb}^S is the number of nearest neighbor atoms for material $S = AX$, BY.

The next assumption of the charge flow model is that the chemical exchange energy $\Delta E_{chem}(\sigma, x)$ for an alloy configuration σ with AX composition x is directly proportional to the deviation of mean charge flow square $\Delta J(\sigma, x)$:

$$\Delta E_{chem}(\sigma, x) = a\Delta J(\sigma, x), \tag{7}$$

and perhaps even for the atomic relaxation, we have:

$$\Delta E_{chem}(\sigma, x) + \Delta E_{rel}(\sigma, x) = b\Delta J(\sigma, x), \tag{8}$$

where a and b are fitting parameters. Note that both ΔE_{chem} and ΔE_{rel} are energy per atom. The charge flows $\{C_{ij}\}$ for a given alloy configuration can be solved from Eq. 5 which is a system of linear equations. There are, however, only N such equations for the $4N$ unknown C_{ij}'s. Using the relation $C_{ij} = -C_{ji}$, we can reduce the number of the unknowns to $2N$. If we require $J(\sigma, x)$ to be minimized under the constraint of Eq. 5, the set of charge flows will have zero circulation, i.e., the sum of charge flows around any loop in the bonding network is 0. Subsequently a single-valued function V can be assigned to each atom such that the charge flow C_{ij} from atom i to j is equal to $V_i - V_j$ (please see Appendix A for proofs). By doing this, we can further reduce the number of the unknowns to N and easily solve for all C_{ij}.

An interesting property of the charge flow model is that the value of ΔJ calculated using a set of atom charges $\{Q_A, Q_X, Q_B, Q_Y\}$ is related to $\Delta J'$ calculated with a different set $\{Q'_A, Q'_X, Q'_B, Q'_Y\}$ as

$$\Delta J' = [(Q'_A - Q'_B)/(Q_A - Q_B)]^2 \Delta J. \tag{9}$$

Note here $Q_A = -Q_X$, $Q_B = -Q_Y$, $Q'_A = -Q'_X$, $Q'_B = -Q'_Y$, $Q_A \neq Q_B$, and $Q'_A \neq Q'_B$. Therefore the model is independent of the exact values of Q_A and Q_B as the prefactor can be absorbed in a and b of Eqs. 7 and 8. Another important result derived from the model is that for any alloy configuration σ with AX composition x the deviation of mean charge flow square is equal to that of the conjugate configuration $\overline{\sigma}$, generated by exchanging A with B and X with Y in configuration σ, i.e.,

$$\Delta J(\sigma, x) = \Delta J(\overline{\sigma}, 1-x). \tag{10}$$

The derivation of these two properties is shown in Appendix B.

We tested the charge flow model on several nonisovalent alloy systems AX/BY of WZ, zinc-blende (ZB), and rocksalt (RS) structures. Supercells of 3×3×3, 2×2×2, 2×2×1, and 2×1×1 in terms of the primitive unit cells were used with periodic boundary conditions. Approximately 100 bulk configurations were used to fit the charge flow model for each system of WZ and RS structures and 400 for ZB structures with the AX composition x ranging from 0 to 1. These configurations were generated by randomly substituting B with A and Y with X. For alloys of binary compounds which can exist in different crystal structures, e.g., RS MgO and WZ AlN, the model was fitted for each of these structure. The alloy lattice parameters (a for ZB and RS, and a, c for WZ) were calculated from the DFT equilibrium values of the end binary compounds using Vegard's Law: $a_i(x) = xa_i^{AX} + (1-x)a_i^{BY}$. Previous work on GaN/ZnO alloys[15] shows that Vegard's law is satisfied well with a deviation less than 0.7%. We also tested the validity of Vegard's law on GaN/ZnO and AlN/ZnO of WZ structure at three ZnO compositions (x = 0.25, 0.50, 0.75) by fully relaxing both the cell shape/volume and the internal atomic positions of configurations in a

$2\times2\times2$ supercell. We found only a small deviation ($\lesssim$0.5% in a and $\lesssim$0.2% in c) from Vegard's law, which corresponds to an average error less than 0.5 meV/atom. The equilibrium lattice constants of the pure binary semiconductors were obtained by DFT calculations whose parameters were the same as those of the alloys described below. The initial configurations of each system constructed as above are also referred as unrelaxed configurations, in contrast to the relaxed ones which were obtained after performing full *ab initio* ionic relaxation for each initial configuration. The *ab initio* total energy of each alloy configuration was calculated using the Vienna Ab Initio Simulation Package (VASP)[44] with the local density approximation of DFT. Pseudopotentials of projector augmented wave (PAW) type were used for all atoms, and the semicore d electrons of Ga, Zn, In, and Cd were included in the valence electrons. A kinetic energy cutoff of 400 eV and a large Monkhorst-Pack k-point mesh were used to ensure the convergence of the total energy. Ionic relaxation was conducted to converge the atomic forces to 0.01 eV/Å.

We calculated the phase diagram of a nonisovalent alloy system of WZ structure described by the charge flow model using parallel tempering MC simulations.[45] The simulation box is of $8\times8\times5$ in terms of primitive unit cells (~ 25 Å on each side and containing 1280 atoms) with periodic boundary conditions. The AX composition x of the simulated systems ranges from 0.025 to 0.5, and the results for the other half of the composition space can be deduced readily because of the x to $1-x$ symmetry in the charge flow model (Eq. 10). For each composition x, 40 Metropolis MC simulations with temperatures from 300 K to 5613 K were run simultaneously with the configurations exchanged between adjacent temperature runs for every 1000 MC moves. In each run, trial configurations were generated by randomly exchanging A with B, X with Y, or a A–X bonded pair with a B–Y bonded pair. Each system was equilibrated for 2×10^8 steps followed by 8×10^8 steps for averaging. The phase boundary of the phase separated and alloying regions was identified by plotting the average constant volume specific heat capacity, $\langle C_v\rangle$, as a function of temperature, as given by

$$\langle C_v\rangle = \frac{\langle E^2\rangle - \langle E\rangle^2}{k_B T^2},$$

where E is the total energy, and k_B is the Boltzmann constant. Peaks in the $\langle C_v\rangle$ versus T diagram were used in the characterization of phase transition.

III. RESULTS AND DISCUSSION

A. Application of Charge Flow Model to Nonisovalent Alloy Systems

In our previous work,[9] we applied the charge flow model to GaN/ZnO alloys of WZ structure and obtained a very good fitting of the *ab initio* chemical exchange energy. In this work, we applied the model on several other nonisovalent alloy systems of various crystal structures, including III-V/II-VI (AlN/ZnO, GaAs/ZnSe, InP/CdS, and AlN/MgO in WZ, GaN/ZnO and GaAs/ZnSe in ZB, and AlN/MgO in RS), and III-V/IV-IV (AlN/SiC in WZ). The fitting results for *ab initio* ΔE_{chem} of these systems including GaN/ZnO in WZ structure are shown in Fig. 1.

From the results, we can see that the *ab initio* ΔE_{chem} of alloy configurations in the entire composition range $0 < x < 1$ are fitted very well by the charge flow model (Eq. 7) for all nonisovalent alloy systems we tested. The standard deviation of the fitting for most systems is less than 10 meV/atom and the coefficient of determination[46] R^2 is very close to 1. The agreement between the model-predicted and *ab initio* ΔE_{chem} is generally better for low-energy configurations than those high-energy ones. This might be due to their different structural characters. The low-energy alloy configurations have more "correct bonds" ($A-X$ and $B-Y$) inherited from the parent materials AX and BY, and less "wrong bonds" ($A-Y$ and $B-X$) resulted from the mixing, thus more resembling the phase separated state and having smaller charge flow deviation. If we consider Eq. 7 as an expansion of ΔE_{chem} in terms of ΔJ up to the first order, such a description will be adequate for these low-energy configurations. In contrast, the high-energy configurations are usually more random in atom arrangement and possess more "wrong bonds". This situation is more impurity-like, e.g., A in BY and X in BY, which are large perturbations from the phase separated state and might require higher-order terms in the energy model. In practice, however, these high-energy configurations will not present a big problem for using the charge flow model in MC simulations, because the statistical weight of these unstable configurations is very small under relevant temperatures (≤ 2000 K).[1]

As shown in our previous work on GaN/ZnO alloys,[9] our charge flow model can also fit the *ab initio* $\Delta E_{chem} + \Delta E_{rel}$ quite accurately (see Fig. 1 in ref. 9). In the current work, a similarly good fitting is found across the entire composition space for GaAs/ZnSe, InP/CdS, and AlN/MgO in WZ, and AlN/MgO in RS. The fitting results of these systems together with GaN/ZnO in WZ are shown in Fig. 2. Interestingly, the relaxation energy ΔE_{rel} by itself agrees quite well with $(b-a)\Delta J$ (see Fig. 3), especially when $|\Delta E_{rel}|$ is small. The data points with larger $|\Delta E_{rel}|$ are more scattered and more deviated from linearity, which is probably due to the larger structural relaxation, as indicated by the larger average bond length change during relaxation ($\langle|\Delta R|\rangle$) (see Fig. 4 for $|\Delta E_{rel}|$ versus $\langle|\Delta R|\rangle$ of GaN/ZnO alloys in WZ structure). We also found a quite good linear relationship between the relaxation energy and the chemical exchange energy, as shown in Fig. 4, suggesting that configurations

with more wrong bonds and hence larger ΔE_{chem} will undergo larger structural relaxation. The linear relationship between ΔE_{rel} and ΔE_{chem} and that between ΔE_{chem} and ΔJ explain the surprisingly good prediction of the relaxation energy by ΔJ, which only depends on alloy atomic configuration on lattice sites.

In the case of AlN/ZnO, the good linearity between ΔE_{chem} and ΔJ across the entire composition space (see Fig. 1) is lost after including the relaxation energy term, as shown in Fig. 5a. For configurations of the same composition, however, the linear relationship is still present (see empty symbols in Fig. 5a), albeit with a nonzero intercept, which can be fitted by a composition-dependent term $c'x(1-x)$:

$$\Delta E_{chem}(\sigma, x) + \Delta E_{rel}(\sigma, x) = b'\Delta J(\sigma, x) + c'x(1-x). \tag{11}$$

The fitting result is shown in Fig. 5b with $b' = 1.1643$ and $c' = -0.4273$ eV/atom. This additional, composition-dependent term accounts for the variation of ΔE_{rel} vs. ΔJ with respect to x, as shown in Fig. 6. The overall $|\Delta E_{rel}|$ versus ΔJ plot has a large scatter. However, if we compare the $|\Delta E_{rel}|$ versus ΔJ data for each composition x, a linear relationship with a similar slope but different intercepts emerges, which justifies the use of the second term in Eq. 11. Note that, since this $c'x(1-x)$ term is the relaxation energy term when $\Delta J = 0$ (i.e., when A and B are separated in a large system), conceptually one might consider it as a relaxation energy term not included in ΔE_{def} in Eq. 2 (which also depends on x). The ΔE_{def} describes the elastic energy relaxation from the reference lattice constants $\{\mathbf{a}_i^{AX}\}$ and $\{\mathbf{a}_i^{BY}\}$ to a Vegard's law lattice constant $\{\mathbf{a}_i(x)\}$ separately for AX and BY. On the other hand, $c'x(1-x)$ might be viewed as describing a coherent AX/BY system, with one part to be AX and the other part to be BY, relaxed from a uniform crystal lattice $\{\mathbf{a}_i(x)\}$ to lower energy structures under the coherent and periodic boundary conditions (e.g., into the Poisson ratio structure). We can hence call it a coherence relaxation energy term. However, the above view is complicated by the fact that the ΔJ term might not be restricted to the interface for such a coherent AX/BY system, hence not increasing proportionally to the volumes of AX and BY. So it cannot be ignored in a large AX/BY coherent system. For example, if AX and BY are connected in the (111) direction in a ZB structure, ΔJ is proportional to the volume of the system (there will be a long range charge flow). As a result, the $c'x(1-x)$ can also contain some chemical binding energies. As for the other alloy systems shown in Fig. 2, a similar term might be able to be used to improve the fitting. Nevertheless, compared to AlN/ZnO, ΔE_{rel} for the other systems is of much smaller magnitude relative to ΔE_{chem} ($\leq 50\%$), $E_{def} + c'x(1-x)$ is positive, and there is a better overall linearity of ΔE_{rel} vs. ΔJ (see Fig. 3). Thus $\Delta E_{chem} + \Delta E_{rel}$ can be fitted with the original one parameter model (Eq. 8) reasonably well without using the composition-dependent term. The relatively much larger ΔE_{rel} of AlN/ZnO alloys compared to the other systems can be explained by the radius difference between the alloy cations: 0.24 Å for Al and Zn, 0.12 Å for Ga and Zn, 0.16 Å for In and Cd, and 0.15 Å for Al and Mg.[47] The much larger radius difference between Al and Zn compared to that between Ga and Zn gives rise to larger relaxation from the initial ideal lattice sites. See Fig. 7 for the mean bond length change and relaxation energy for these two alloy systems using the same configurations generated from Al→Ga substitutions.

The predictive ability of the charge flow model for new alloy configurations is evaluated on a set of test configurations that were not included in the fitting set. For each nonisovalent alloy system of WZ structure, we consider 15, 14, and 3 configurations in the 2×2×2, 3×3×3, and 4×4×4 supercells, respectively; for each alloy of RS structure, we consider 15 and 3 configurations in the 2×2×1 and 3×3×3 supercells, respectively; for each alloy of ZB structure, we consider 15 and 3 configurations in the 2×2×2 and 3×3×3 supercells, respectively. For GaN/ZnO of WZ structure, we also included four configurations of a 8×8×5 supercell obtained from MC simulations at the starting point and after equilibration at 300 K, 1100 K, and 1500 K, respectively, the former three of which were also reported in Fig. 1 in our previous work for GaN/ZnO.[9] The root mean square (rms) deviations of the model-predicted ΔE_{chem} and $\Delta E_{chem} + \Delta E_{rel}$ from the LDA values are shown in Table I. The data points of the test configurations of the largest supercell for each alloy system are also shown in Figs. 1 and 2. The agreement of the model-predicted energies with the LDA calculated energies for the test configurations is very good, comparable to those of the fitting configurations. The good agreement for the large supercell results indicates that the charge flow model can take into account of long range interactions correctly. Despite that all structures in the training set were generated by random substitution and no structures with short range ordering and long range ordering (e.g., superlattices) were deliberately included, some ordering effects were implicitly accounted for in the model to some extent in terms of the artificial periodicity introduced by the small size of the supercells of the training structures. What's more, our model thus fitted can accurately predict the formation enthalpy of structures with phase separation (300 K MC snapshot), with short range ordering (1100 K and 1500 K MC snapshots), and with no ordering (initial MC configuration) (cf. filled symbols in Fig. 2). However, we will investigate in the future for how well our model predicts the energies of highly ordered structures like superlattices (where long range elastic effects might exist), and whether such highly ordered structure data need to be included in the model.

The first term in Eq. 1, ΔE_{def}, is always positive because the lattice parameters of the alloy are usually not those of the base materials and the resulting deformation costs energy. If the lattice mismatch of AX and BY is not very big, the contribution of ΔE_{def} can be quite small: e.g., for GaN/ZnO with ∼1.3 % mismatch, it is less than 2 meV/atom. If the lattice mismatch is big, like AlN/ZnO (∼4.2 %), however, this term can be as large as 18 meV/atom. The second term ΔE_{chem}, as shown in Fig. 1, is always positive for all the systems we tested, reflecting the larger affinity between atoms from the same base material. If we only consider contributions from the first two terms, the mixing enthalpy ΔH_{mix} will be positive and therefore a high temperature is needed for alloy formation. The third term, ΔE_{rel}, is always negative and thus reduces the mixing enthalpy and decreases the

TABLE I: rms deviation of the model-predicted ΔE_{chem} and $\Delta E_{chem} + \Delta E_{rel}$ from the LDA values for test configurations not included in the fitting set. Units in meV/atom.

system	rms (ΔE_{chem})	rms ($\Delta E_{chem} + \Delta E_{rel}$)
GaN/ZnO (WZ)	8.8	9.8
GaN/ZnO (ZB)	4.5	-
AlN/ZnO (WZ)	7.9	16.6[a]
AlN/SiC (WZ)	23.3	-
AlN/MgO (WZ)	29.7	23.3
AlN/MgO (RS)	17.1	14.8
GaAs/ZnSe (WZ)	16.7	10.9
GaAs/ZnSe (ZB)	6.7	-
InP/CdS (WZ)	6.4	4.7

[a] Model-predicted values are calculated with Eq. 11.

miscibility temperature. If $|\Delta E_{rel}|$ is large enough, it could even lead to negative ΔH_{mix} and cause spontaneous alloy formation at 0 K. As we can see from the results, ΔE_{rel} for all systems except AlN/ZnO is not negative enough to counter the effect of positive ΔE_{chem}, thus making $\Delta H_{mix} > 0$. This is consistent with the experimental observation that high temperatures are required in the synthesis of GaN/ZnO (>1000 K)[4,5] and AlN/SiC (>1800 K)[1] alloys. In contrast, AlN/ZnO alloys undergo much larger relaxation such that the relaxation energy ΔE_{rel} for some configurations is comparable or even larger than the chemical exchange energy ΔE_{chem} in magnitude (see Fig. 6). The sum of these two terms can be as negative as ~ -50 meV/atom. Even after taking into account of the positive ΔE_{def} which is 18 meV/atom at most, the mixing enthalpy could become negative for some of these configurations (for an intermediate size or mixed system). Therefore, the spontaneous formation of AlN/ZnO alloys of certain compositions can be expected. Note here that for alloy structures of the same composition, those with negative formation enthalpy have more ordering (i.e., smaller ΔJ) than those with positive formation enthalpy (cf. Eq. 11). Random structures with no ordering all have very positive formation enthalpy.

We also tried to use the Ewald energy of the unrelaxed configurations to fit the *ab initio* ΔE_{chem} and $\Delta E_{chem} + \Delta E_{rel}$. If assuming the charge on each ion is its valence charge, the Ewald energy model can be written as

$$\begin{aligned}\Delta E_{chem}(\sigma, x) &= f\Delta E_{ew}(\sigma, x) = f\left\{\sum_{i<j}^{N} \frac{Q_i Q_j}{r_{ij}}\right. \\ &\left. -[xE_{ew}^{AX}(\{\mathbf{a}_i(x)\}) + (1-x)E_{ew}^{BY}(\{\mathbf{a}_i(x)\})]\right\}, \end{aligned} \tag{12}$$

$$\Delta E_{chem}(\sigma, x) + \Delta E_{rel}(\sigma, x) = f'\Delta E_{ew}(\sigma, x) \tag{13}$$

where ΔE_{ew} is the unscreened Ewald energy, f and f' are fitting parameters, and $E_{ew}^{AX}(\{\mathbf{a}_i(x)\})$ and $E_{ew}^{BY}(\{\mathbf{a}_i(x)\})$ are the Ewald energies of AX and BY with the lattice parameters $\{\mathbf{a}_i(x)\}$ for alloys of AX composition x. The fitting results for GaN/ZnO in WZ structure are shown in Fig. 8. Compared to the charge flow model, the fitting of the Ewald energy model is slightly worse in both cases with the error $\sim$1.5 times larger. Interestingly, the Ewald energy can be fitted with ΔJ quite accurately (see Fig. 9), suggesting a connection between these two models. First, these two models both assume fixed point charges on ions (which can be relaxed by allowing environment-dependent charges as in ref. 33). Second, more importantly, the local charge balance principle, an extension of Pauling's electrostatic valence rule,[42] can be considered as the underlying driver to lower the energy in both charge flow model and the Ewald energy model, which might explain their strong correlation shown in Fig. 9. Compared to the qualitative Pauling's rule, the charge flow model provides a quantitative number for the chemical binding. Note that, mathematically, the charge flow model and Ewald energy model are not equivalent (cf. Fig. 9). While the charge flow model uses the bonding topology as the input, the Ewald energy model uses the physical atomic positions. While the former deals more with the chemical binding, the latter deals more with the electrostatic energy. We do find that in most cases, we can use both energy terms with two fitting parameters to get a much better fitted results.

B. Phase Diagram of Nonisovalent Alloys

The stability of nonisovalent alloys depends on both the mixing enthalpy and entropy. From the last subsection, we can see that ΔH_{mix} is always positive for all these alloy systems except AlN/ZnO. This means that the formation of these alloys except

AlN/ZnO is not favored at 0 K. As the temperature increases, the effect of ΔS_{mix} becomes more and more important and ΔG_{mix} becomes less and less positive. The formation of alloys will only be spontaneous at temperature $T > \Delta H_{mix}/\Delta S_{mix}$. The calculation of ΔS_{mix}, however, is not a trivial task, especially for large systems, and when short range order is involved. Here we use Monte Carlo simulations to locate the phase transitions and plot the phase diagram of nonisovalent alloy systems of WZ structure whose energy can be described by the charge flow model. The parallel tempering technique is used to improve convergence of the simulations, especially those at relatively low temperatures and near the phase boundaries.[45] The calculated phase diagram is shown in Fig. 10. Here, instead of specifying a particular system, we use a reduced temperature T^*, defined as $T^* = T/b$, where b is the fitting parameter in the charge flow model for $\Delta E_{chem} + \Delta E_{rel}$ in Eq. 8 with $Q_A = +3$, $Q_B = +2$. The value of b for each system can be found in Figs. 1 and 2 and scaled using Eq. 9. Since b is in the order of unity for all systems tested in this work, for simplicity, we only use its value to calculate T^* which then has the unit of K. The plot of the average constant volume specific heat capacity versus temperature for $x = 0.5$ is shown in Fig. 11. No appreciable changes in the results were found when the size of the supercell is increased to 13×13×8 primitive unit cells, which is ∼41 Å on each side and contains 5408 atoms.

From the phase diagram, we can see that the two semiconductors AX and BY remain phase separated under the curve, while above the curve, they can be mixed together, but with short range order, i.e., clustering of the material of less amount in the other. The snapshots of the equilibrated configurations for $x = 0.25$ at 664 K and 1100 K are shown in Fig. 12 to illustrate these two phases. The quantitative characteristics of the atomic configurations in these two regions can also be seen clearly in the radial distribution function for A–X shown in Fig. 13. The transition from the phase separated state to the alloying state appears to be first order, as judged from the $\langle C_v \rangle$ versus T^* plots (see Fig. 11). The phase diagram is symmetric with respect to $x = 0.5$, due to the inherent symmetry in the charge flow model (Eq. 10). The temperature at the phase boundary, i.e., the miscibility temperature, is raised from ∼680 K to ∼880 K as the AX composition x increases from 0.025 to 0.5. This trend can be explained in this way: alloying will create new interfaces between AX and BY accompanied by more $A - Y$ and $B - X$ "wrong bonds" which have higher energies; the more AX there is to be mixed with BY, the higher energy is needed, and thus the higher miscibility temperature is required. Further increase of x above 0.5 will lower the miscibility temperature because this situation can be regarded as mixing BY in AX with BY composition $1 - x$. If the temperature is raised high enough, the clustering can be removed and a homogeneous random alloy can be formed. However, this is not reached even at 5613 K, the highest simulation temperature in this work. Thus, the completely random configurations assumed by some previous calculations for nonisovalent alloy systems are not good structure models under the synthesis conditions, which have temperatures lower than 2000 K.[1,4,5]

IV. CONCLUSION

In this work, we extended the charge flow model proposed in our previous paper[9] and applied it to a number of nonisovalent alloy systems. Good agreement between the DFT total energies and the model-predicted values was found, thus indicating the wide applicability of the model. We also used the model to study the thermodynamic properties of nonisovalent alloys of WZ structure and obtained a general phase diagram and the ordering functions which can be used to guide the synthesis of new alloy systems.

Acknowledgements

This work was performed in the Helios Solar Energy Research Center which is supported by the Director, Office of Science, Office of Basic Energy Sciences, Materials Science and Engineering Division, of the U.S. Department of Energy (DOE) under Contract No. DE-AC02-05CH11231. This research used the computational resources of the National Energy Research Scientific Computing Center (NERSC) and the National Center for Computational Sciences (NCCS), with the computational time allocated by the Innovative and Novel Computational Impact on Theory and Experiment (INCITE) project, of DOE.

Appendix A: Proofs Needed for Solving Local Charge Balance Equations

For a loop K in the bonding topology, we define the circulation of the charge flows $\{C_{ij}\}$ on K as

$$\Gamma(K) \equiv \sum_{i\text{-}j \in K} C_{ij}.$$

Suppose the charge flows $\{C_{ij}\}$ satisfy Eq. 5, and the circulation on one loop K is not zero. Then we can construct a new set of charge flows $\{C'_{ij}\}$ with $C'_{ij} = C_{ij} - \Gamma(K)/N_b(K)$ for i-$j \in K$ and $C'_{ij} = C_{ij}$ for i-$j \notin K$, where $N_b(K)$ is the number

of bonds on loop K. For $\{C'_{ij}\}$ constructed in this way, the circulation on loop K is zero and Eq. 5 is also satisfied. The mean charge flow square of the new charge flows is

$$\begin{aligned} J' &= \frac{1}{N}\sum_{i=1}^{N}\sum_{i\sim j}(C'_{ij})^2 \\ &= \frac{2}{N}\left\{\sum_{\substack{i\sim j \\ i\text{-}j\notin K}} C_{ij}^2 + \sum_{i\text{-}j\in K}\left[C_{ij}-\frac{\Gamma(K)}{N_b(K)}\right]^2\right\} \\ &= \frac{2}{N}\sum_{i\sim j} C_{ij}^2 + \frac{2}{N}\sum_{i\text{-}j\in K}\left\{\left[C_{ij}-\frac{\Gamma(K)}{N_b(K)}\right]^2 - C_{ij}^2\right\} \\ &= J - \frac{2\Gamma^2(K)}{NN_b(K)}. \end{aligned}$$

We can see that J' is always smaller than J as long as the circulation of the original set of charge flows $\{C_{ij}\}$ on loop K is not zero. Therefore the set of charge flows with the minimal J must have zero circulation on all loops.

Now we need to prove that such an all-zero-circulation set of charge flows is unique. For a given set of charge flows $\{C_{ij}\}$ on the bonding topology graph, let's start with atom 1 and cut bonds to break all loops to generate an open, but connected graph (tree structure) (see Fig. 14). Then we can define on each tree node (atom) i a function V with $V_1 = 0$ and $V_i = V_j + C_{ij}$, where j is the parent of node i in the tree graph. Now defining $C'_{ij} = V_i - V_j$ for all i, j connected in the original graph, we will first show that C'_{ij} is just C_{ij}. If i-j is an edge of the tree graph, then $C_{ij} = C'_{ij}$ by definition. If i-j is a cleaved bond (dashed line in Fig. 14), connecting i and j will form a loop K on which $\Gamma(K) = 0$ and $\Gamma'(K) = \sum_{i'\text{-}j'\in K} C'_{i'j'} = \sum_{i'\text{-}j'\in K}(V'_{i'} - V'_{j'}) = 0$. All the other edges i'-j' of K are on the tree graph, and thus $C'_{i'j'} = C_{i'j'}$. So we have $C_{ij} = C'_{ij}$ for this cleaved bond.

In this way, we have shown that, for any $\{C_{ij}\}$ with all zero circulations, we can construct $\{V_i\}$, where $C_{ij} = V_i - V_j$ and also satisfy Eq. 5. Now, we have equal number of V_i ($V_1 = 0$) and local charge balance equations (Eq. 5). So we can uniquely solve for $\{V_i\}$, which also uniquely define $\{C_{ij}\}$.

Appendix B: Important Properties of Charge Flow Model

We will derive here two important properties of the charge flow model, Eqs. 9 and 10. Here we will assume the crystal structure is WZ with $N_{nnb} = 4$. The derivation is similar for other crystal structures. Consider two sets of atomic charges $\{Q_i^{(a)}\}$ and $\{Q_i^{(c)}\}$, in which Q_A, Q_X, Q_B, Q_Y (charges on atoms A, X, B, and Y) are +1,-1,+1,-1 and +1,-1,0,0, respectively. Using the same convention as in the text, all cations (A and B) are indexed from 1 to $N/2$, and all anions (X and Y) $N/2+1$ to N. For $\{Q_i^{(a)}\}$, using the symmetry argument, we have

$$C_{ij}^{(a)} = \begin{cases} \frac{1}{4} & i\sim j, i\le N/2, \\ -\frac{1}{4} & i\sim j, i > N/2, \\ 0 & \text{otherwise.} \end{cases}$$

On the other hand, $C_{ij}^{(c)}$ depends on the atomic configuration σ and thus has to be calculated by solving Eq. 5 with the corresponding set of charges $Q^{(c)}$, in contrast to the simple form of $C_{ij}^{(a)}$.

Consider an arbitrary set of atomic charges $\{Q_i^{(e)}\}$ with Q_A, Q_X, Q_B, Q_Y equal to $d+f$, $-d-f$, f, $-f$, respectively. Note here $d = Q_A - Q_B$. Then we have $Q_i^{(e)} = fQ_i^{(a)} + dQ_i^{(c)}$ and also $C_{ij}^{(e)} = fC_{ij}^{(a)} + dC_{ij}^{(c)}$. The mean charge flow square is then

$$\begin{aligned} J^{(e)} &= \frac{1}{N}\sum_{i=1}^{N}\sum_{i\sim j}(C_{ij}^{(e)})^2 \\ &= \frac{f^2}{4} + d^2J^{(c)} + \frac{2fd}{N}\sum_{i=1}^{N}\sum_{i\sim j} C_{ij}^{(a)}C_{ij}^{(c)}. \end{aligned} \tag{B1}$$

The last term on the right hand side of the above equation can be simplified as

$$\begin{aligned} & \frac{2fd}{N}\sum_{i=1}^{N}\sum_{i\sim j}C_{ij}^{(a)}C_{ij}^{(c)} \\ = & \frac{2fd}{4N}\left(\sum_{\substack{i\le N/2\\ i\sim j}}C_{ij}^{(c)}-\sum_{\substack{i>N/2\\ i\sim j}}C_{ij}^{(c)}\right) \\ = & \frac{fd}{2N}\left(\sum_{i\le N/2}Q_i^{(c)}-\sum_{i>N/2}Q_i^{(c)}\right) \\ = & \frac{xfd}{2}, \end{aligned} \tag{B2}$$

where x is the composition of AX in the alloy. Substituting Eq. B2 into Eq. B1 yields

$$J^{(e)} = \frac{f^2}{4}+d^2J^{(c)}+\frac{xfd}{2}.$$

For the phase separated state, we have

$$\begin{aligned} & xJ(AX)+(1-x)J(BY) \\ = & \frac{x(d+f)^2}{4}+\frac{(1-x)f^2}{4}. \end{aligned}$$

So the deviation of the mean charge flow square of an alloy configuration from the phase separated state is

$$\begin{aligned} \Delta J &= J^{(e)}-[xJ(AX)+(1-x)J(BY)] \\ &= d^2(J^{(c)}-\frac{x}{4}) \\ &= (Q_A-Q_B)^2(J^{(c)}-\frac{x}{4}) \end{aligned} \tag{B3}$$

which is proportional to $(Q_A-Q_B)^2$.

For a configuration σ of AX composition x with atomic charges $\{Q_i^{(e)}\}$, the conjugate configuration $\overline{\sigma}$, generated by exchanging A with B and X with Y, has a AX composition $1-x$, and atomic charges $\{Q_i^{(f)}\}$ which are equivalent to $\{Q_i^{(e)}\}$ with the values of Q_A, Q_X, Q_B, Q_Y reassigned to f, $-f$, $d+f$, $-d-f$, respectively. So according to the above formula,

$$\begin{aligned} \Delta J(\overline{\sigma},1-x) &= [f-(d+f)]^2(J^{(c)}-\frac{x}{4}) \\ &= \Delta J(\sigma,x). \end{aligned}$$

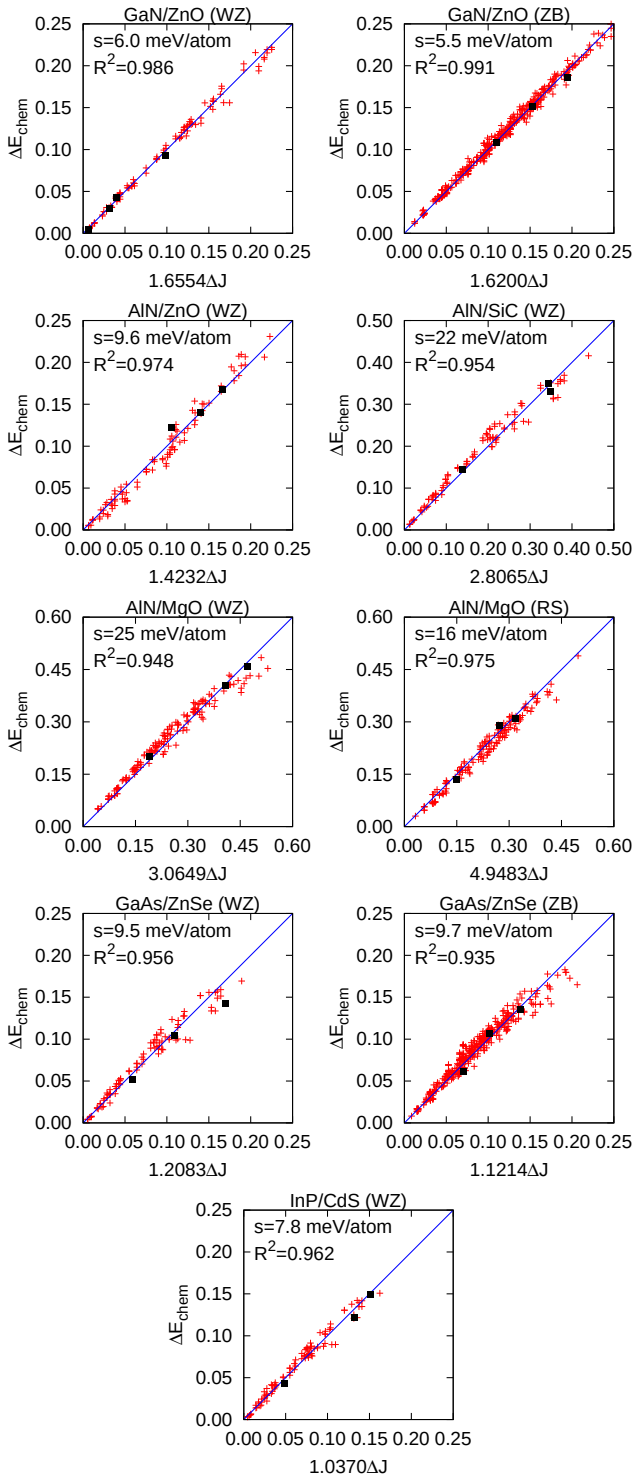

FIG. 1: Fitting of the *ab initio* ΔE_{chem} (in eV/atom) by $a\Delta J$. The value of the fitting parameter a is given in the label of the x axis. Each cross represents one fitting configuration. The solid line represents an exact agreement. Filled squares: test configurations of the largest supercell not included in the fitting set. The charges are $+3$ for Al, Ga, In, $+2$ for Mg, Zn, Cd, -3 for N, P, As, and -2 for O, S, Se.

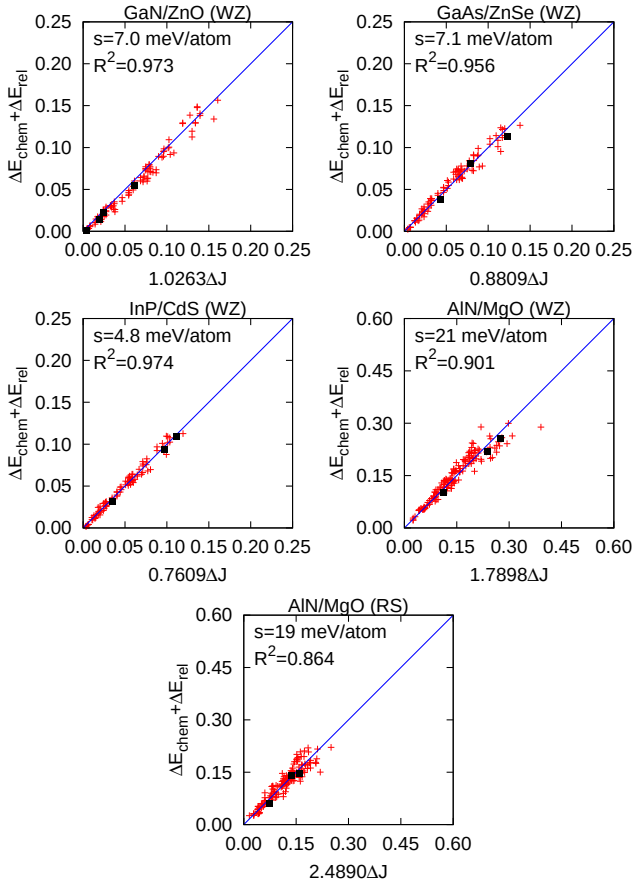

FIG. 2: Fitting of the *ab initio* $\Delta E_{chem} + \Delta E_{rel}$ (in eV/atom) by $b\Delta J$. The value of the fitting parameter b is given in the label of the x axis. Please see the caption of Fig. 1 for the legend.

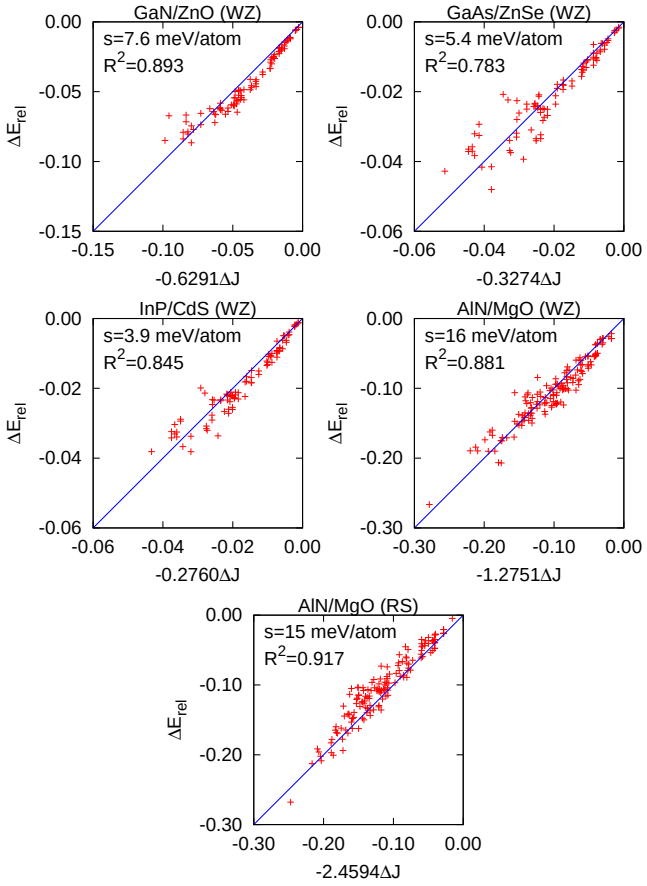

FIG. 3: Comparison of the *ab initio* ΔE_{rel} (in eV/atom) with $(b-a)\Delta J$. The value of $b-a$ is given in the label of the x axis. Please see the caption of Fig. 1 for the legend.

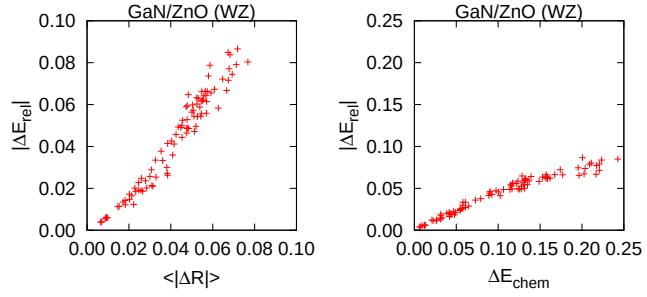

FIG. 4: Comparison of the *ab initio* $|\Delta E_{rel}|$ (in eV/atom) with $\langle|\Delta R|\rangle$, the average bond length change (in Å) in the left panel and with ΔE_{chem} (in eV/atom) in the right panel for GaN/ZnO alloys of WZ structure. Each cross represents one fitting configuration.

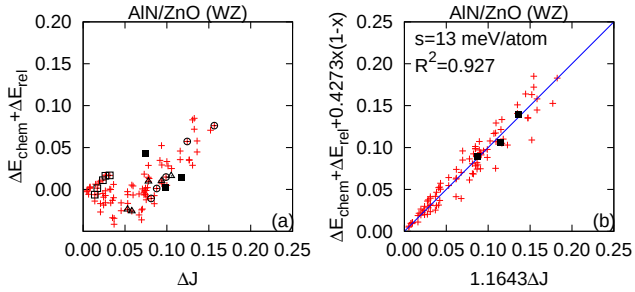

FIG. 5: Fitting of the *ab initio* $\Delta E_{chem} + \Delta E_{rel}$ (in eV/atom) by ΔJ for AlN/ZnO of WZ structure. Each cross represents one fitting configuration. Empty squares, empty triangles, and empty circles: fitting configurations of composition $x = 0.0625, 0.5, 0.8125$, respectively. Filled squares: test configurations of the 4×4×4 supercell. The solid line represents an exact agreement.

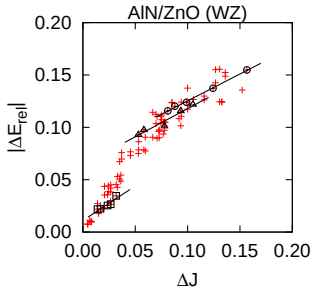

FIG. 6: *Ab initio* $|\Delta E_{rel}|$ (in eV/atom) versus ΔJ for AlN/ZnO of WZ structure. Each cross represents one fitting configuration. Data for configurations with composition $x = 0.0625, 0.5, 0.8125$ are highlighted with empty squares, circles, and triangles, respectively, together with the corresponding solid fitting lines.

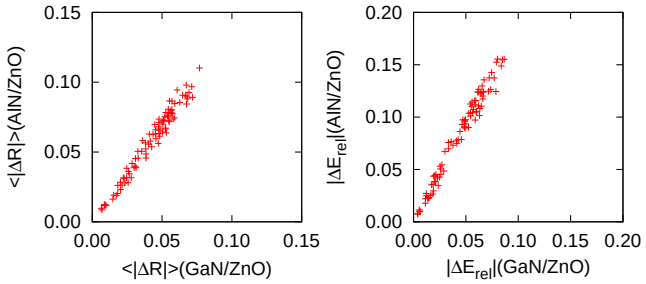

FIG. 7: Fitting of $\langle|\Delta R|\rangle$ (left) and $|\Delta E_{rel}|$ (right) of AlN/ZnO with that of GaN/ZnO for the same configurations. Each cross represents one fitting configuration. Bond lengths in Å. Energies in eV/atom.

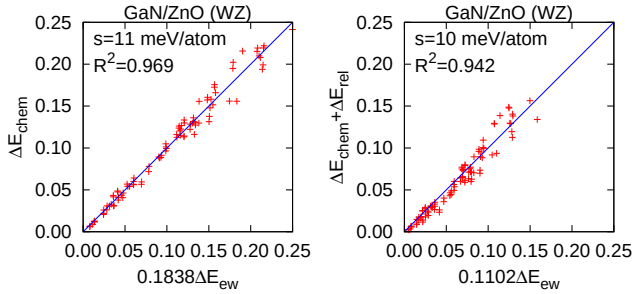

FIG. 8: Fitting of the *ab initio* ΔE_{chem} by $f\Delta E_{ew}$ (left) and $\Delta E_{chem} + \Delta E_{rel}$ by $f'\Delta E_{ew}$ (right) for GaN/ZnO alloys of WZ structure. The values of f and f' are in the labels for the x axis. Please see the caption of Fig. 1 for the legend.

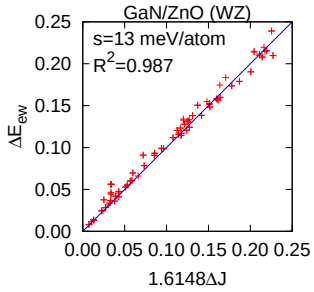

FIG. 9: Fitting of ΔE_{ew} (in eV/atom) by ΔJ for unrelaxed configurations of GaN/ZnO in WZ structure. Please see the caption of Fig. 1 for the legend.

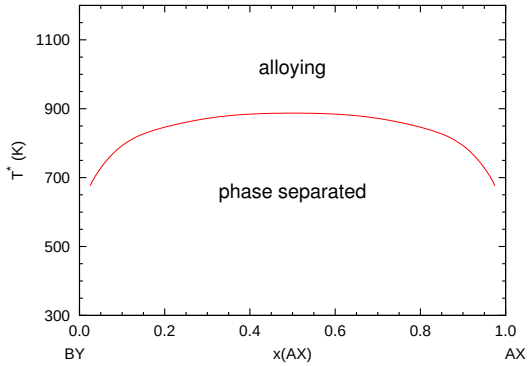

FIG. 10: Phase diagram of reduced temperature T^* vs. AX composition x for nonisovalent alloy AX/BY of WZ structure.

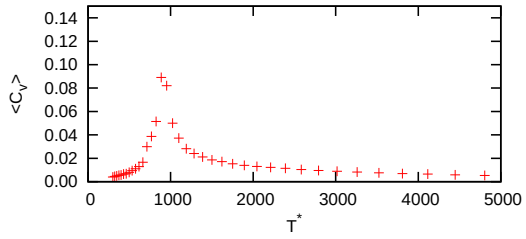

FIG. 11: Average constant volume specific heat capacity $\langle C_v \rangle$ (in meV/atom·K) versus reduced temperature T^* (in K) for $x = 0.5$.

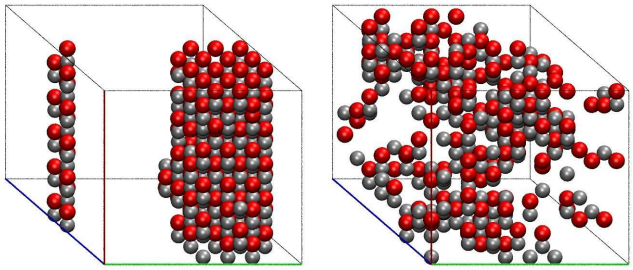

FIG. 12: Snapshots of PTMC simulations of nonisovalent alloy AX/BY of WZ structure with AX composition $x = 0.25$ at $T^* = 664$ K and 1100 K. A: silver. X: red. B and Y atoms are not shown.

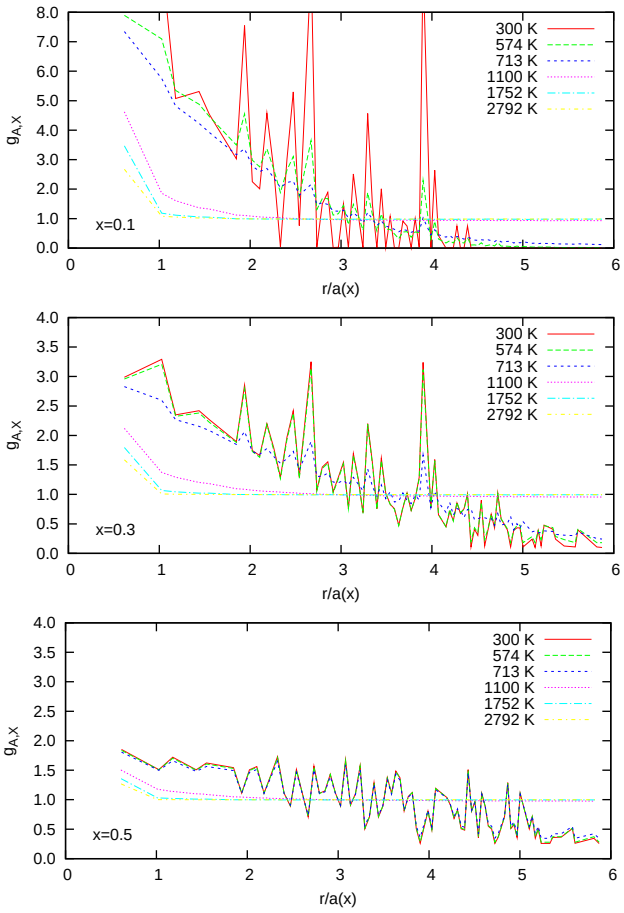

FIG. 13: A–X radial distribution function for nonisovalent alloy AX/BY of WZ structure with AX composition $x = 0.1$, 0.3, 0.5 at several reduced temperatures. The A–X distance r is normalized with respect to the alloy lattice constant $a(x)$. Long range ordering (oscillation in the radial distribution function) is observed when T^* is lower than the miscibility temperature.

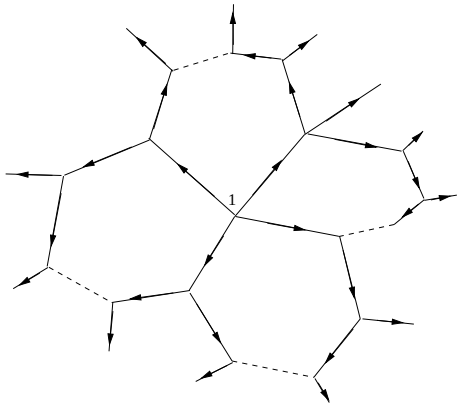

FIG. 14: Scheme of generating a tree structure from the original bonding network by breaking bonds (dashed lines). The root of the tree is atom 1. Charge flows: arrows.

* Electronic address: swang2@lbl.gov

[1] I. B. Cutler, P. D. Miller, W. Rafaniello, H. K. Park, D. P. Thompson, and K. H. Jack, Nature **275**, 434 (1978).
[2] A. Zunger, S. Wagner, and P. M. Petroff, J. Electro. Mater. **22**, 3 (1993).
[3] W. M. Yim, J. Appl. Phys. **40**, 2617 (1969).
[4] K. Maeda, T. Takata, M. Hara, N. Saito, Y. Inoue, H. Kobayashi, and K. Domen, J. Am. Chem. Soc. **127**, 8286 (2005).
[5] K. Maeda, K. Teramura, D. Lu, T. Takata, N. Saito, Y. Inoue, , and K. Domen, Nature **440**, 295 (2006).
[6] J.-F. Li and R. Watanabe, J. Mater. Sci. **26**, 4813 (1991).
[7] Y. Lee, H. Terashima, Y. Shimodaira, K. Teramura, M. Hara, H. Kobayashi, K. Domen, and M. Yashima, J. Phys. Chem. C **111**, 1042 (2007).
[8] M. Glicksman and W. D. Kraeft, Solid State Electron. **28**, 151 (1985).
[9] S. Wang and L.-W. Wang, Phys. Rev. Lett. **104**, 065501 (2010).
[10] S. A. Barnett, M. A. Ray, A. Lastras, B. Kramer, J. E. Greene, P. M. Raccah, and L. L. Abels, Electron. Lett. **18**, 891 (1982).
[11] K. E. Newman, A. Lastras-Martinez, B. Kramer, S. A. Barnet, M. A. Ray, J. D. Dow, J. E. Greene, and P. M. Raccah, Phys. Rev. Lett. **50**, 1466 (1987).
[12] K. E. Newman and J. D. Dow, Phys. Rev. B **27**, 7495 (1983).
[13] N. B. Chen and C. H. Sui, Mater. Sci. Eng. B **126**, 16 (2006).
[14] L. G. Wang and A. Zunger, Phys. Rev. B **68**, 125211 (2003).
[15] L. L. Jensen, J. T. Muckerman, and M. D. Newton, J. Phys. Chem. C **112**, 3439 (2008).
[16] W. Wei, Y. Dai, K. Yang, M. Guo, and B. Huang, J. Phys. Chem. C **112**, 15915 (2008).
[17] M. N. Huda, Y. Yan, S.-H. Wei, and M. M. Al-Jassim, Phys. Rev. B **78**, 195204 (2008).
[18] H. Chen, W. Wen, Q. Wang, J. C. Hanson, J. T. Muckerman, E. Fujita, A. I. Frenkel, and J. A. Rodriguez, J. Phys. Chem. C **113**, 3650 (2009).
[19] S.-H. Wei, L. G. Ferreira, J. E. Bernard, and A. Zunger, Phys. Rev. B **42**, 9622 (1990).
[20] P. N. Keating, Phys. Rev. **145**, 637 (1966).
[21] R. M. Martin, Phys. Rev. B **1**, 4005 (1970).
[22] K. Biswas, A. Fraceschetti, and S. Lany, Phys. Rev. B **78**, 085212 (2008).
[23] K. Biswas and S. Lany, Phys. Rev. B **80**, 115206 (2009).
[24] L. Bellaiche, S.-H. Wei, and A. Zunger, Phys. Rev. B **56**, 13872 (1997).
[25] T. Mattila and A. Zunger, J. Appl. Phys. **85**, 160 (1999).
[26] Y. Zhang, A. Mascarenhas, and L. W. Wang, Phys. Rev. B **64**, 125207 (2001).
[27] O. Rubel, K. Volz, T. Torunski, S. D. Baranovskii, F. Grosse, and W. Stolz, Appl. Phys. Lett. **85**, 5908 (2004).
[28] J. W. D. Connolly and A. R. Williams, Phys. Rev. B **27**, 5169 (1983).
[29] L. G. Ferreira, S.-H. Wei, and Z. Zunger, Phys. Rev. B **40**, 3197 (1989).
[30] D. B. Laks, L. G. Ferreira, S. Froyen, and A. Zunger, Phys. Rev. B **46**, 12587 (1992).
[31] B. P. Burton, A. van de Walle, and U. Kattner, J. Appl. Phys. **100**, 113528 (2006).
[32] J. Z. Liu and A. Zunger, Phys. Rev. B **77**, 205201 (2008).
[33] R. Magri, S.-H. Wei, and A. Zunger, Phys. Rev. B **42**, 11388 (1990).
[34] M. van Schilfgaarde, A.-B. Chen, and A. Sher, Phys. Rev. Lett. **57**, 1149 (1986).
[35] R. Osório, S. Froyen, and A. Zunger, Phys. Rev. B **43**, 14055 (1991).
[36] R. Dickman and G. Stell, AIP Conf. Proc. **492**, 225 (1999).
[37] A. B. Walker and M. J. Gillan, J. Phys. C **16**, 3025 (1983).
[38] L. Bellaiche and D. Vanderbilt, Phys. Rev. Lett. **81**, 1318 (1998).
[39] F. Bresme, C. Vega, and J. L. F. Abascal, Phys. Rev. Lett. **85**, 3217 (2000).
[40] K. Hoang, K. Desai, and S. D. Mahanti, Phys. Rev. B **72**, 064102 (2005).
[41] G. P. Srivastava, J. L. Martins, and A. Zunger, Phys. Rev. B **31**, 2561 (1985).
[42] Pauling, *The Nature of the Chemical Bond* (Cornell University Press, Ithaca, NY, 1960), 3rd ed.
[43] M. D. Pashley, Phys. Rev. B **40**, 10481 (1989).
[44] G. Kresse and J. Furthmuller, Comput. Mater. Sci. **6**, 15 (1996).
[45] U. H. E. Hansmann, Chem. Phys. Lett. **281**, 140 (1997).
[46] The coefficient of determination R^2 is defined as $R^2 \equiv 1 - \sum_i (y_i - f_i)^2 / \sum_i (y_i - \overline{y}^2)$, where y_i are the reference values to fit, $\overline{y}$ is their mean, and f_i are the model-predicted values. In the charge flow model, R^2 equals the square of the correlation coefficient between the reference and model-predicted values.
[47] Ionic radii data are obtained from Charles Kittel, *Introduction to Solid State Physics* (John Wiley & Sons, Inc, Hoboken, NJ, 2005), 8th ed. Al 0.50Å, Zn 0.74 Å, Ga 0.62 Å, Mg 0.65 Å, Cd 0.97 Å, In 0.81 Å.